

NUMERICAL ALGORITHMS FOR SIMULATION OF MULTISECTION LASERS BY USING TRAVELING WAVE MODEL

R. ČIEGIS¹, M. RADZIUNAS² and M. LICHTNER²

¹*Vilnius Gediminas Technical University*

Saulėtekio al. 11, LT-10223, Vilnius, Lithuania

E-mail: rc@fm.vgtu.lt

²*Weierstrass Institute for Applied Analysis and Stochastics*

Mohrenstarsse 39, 10117 Berlin, Germany

E-mail: lichtner@wias-berlin.de; radziunas@wias-berlin.de

Received November 8, 2007; revised March 7, 2008; published online September 9, 2008

Abstract. Sequential and parallel algorithms for the simulation of the dynamics of high-power semiconductor lasers is presented. The model equations describing the multisection broad-area semiconductors lasers are solved by the finite difference scheme, which is constructed on staggered grids. This nonlinear scheme is linearized applying the predictor-corrector method. The algorithm is implemented by using the ParSol tool of parallel linear algebra objects. For parallelization we adopt the domain partitioning method, the domain is split along the longitudinal axis. Results of computational experiments are presented, the obtained speed-up and efficiency of the parallel algorithm agree well with the theoretical scalability analysis.

Key words: finite-difference method, parallel algorithms, mathematical modelling, dynamics of lasers.

1 Introduction

High power high brightness edge-emitting semiconductor lasers are compact devices and can serve a key role in different laser technologies such as free space communication [10], optical frequency conversion [26], printing, marking materials processing [33], or pumping fiber amplifiers [29].

A high quality beam can be relatively easy obtained in the semiconductor laser with narrow width waveguide, where the lateral mode is confined to the stripe center. The dynamics of such lasers can be appropriately described by the Traveling Wave (TW) (1+1)-D model [5], that is a system of first-order PDEs with temporal and single (longitudinal) spatial dimension taken

into account. Besides rather fast numerical simulations this model admits also more advanced optical mode – [32] and numerical bifurcation analysis [31], that has proved to be very helpful when tailoring multisection lasers for specific applications. However, the beam power generated by such lasers usually can't exceed few hundreds of miliwats, what is not sufficient for the applications mentioned above.

The required high output power from a semiconductor laser can be easily obtained by increasing its pumped stripe width. Unfortunately, such broad-area lasers are known to exhibit lateral and longitudinal mode instabilities, resulting in filamentations [27] which degrade the beam quality. To achieve an appropriate beam quality while keeping the beam power high one should optimize the broad stripe laser parameters [24] or consider some more complex structures.

We investigate a laser device consisting of an index guided distributed feedback (DFB) ridge-waveguide (RW) master oscillator (MO) and the gain-guided tapered power amplifier (PA) parts. A schematic view of such MOPA device is shown in Fig. 1.

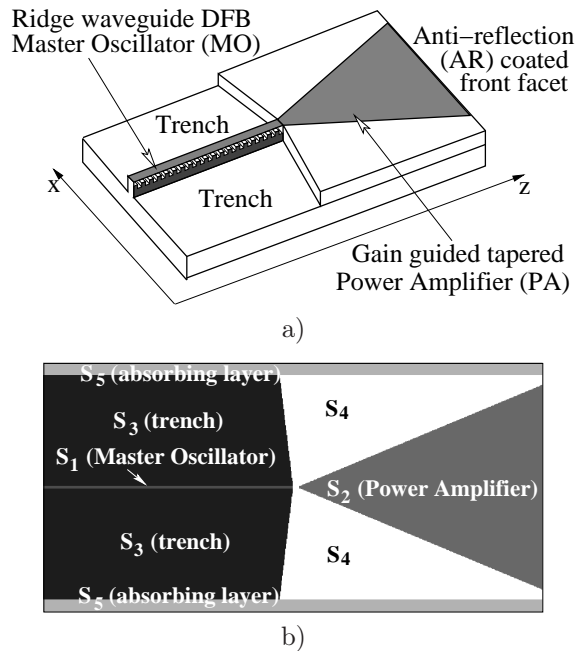


Figure 1. MOPA device: a) schematic view of DFB tapered MOPA, b) division of the spatial domain of computations into five different regions S_1 – S_5 .

The MO (S_1) and the PA (S_2) parts of this device possess metallic contacts and are electrically injected. The outer part of the PA section (S_4) has the same properties as the PA, but has no contact nor current injection. The trench (S_3) part of the device provides a refractive index step, what guarantees a wave-guiding of electrical fields in the ridge waveguide MO (S_1). The lateral size of computational domain $x \in [-X, X] \subset \mathbf{R}$ should be larger than the width

of the MO and the PA parts. The absorbing layers (S_5) are introduced in order to prevent the artificial reflection or transmission of the fields and carriers at the boundaries $x = \pm X$.

However, even in such devices the problem of lateral mode interaction and instability is not solved: in the narrow MO part generated and laterally confined field is directed into the broad PA, which amplifies the beam but can also cause its filamentation and, therefore, should be optimized [3, 8, 36, 38].

There exist different models describing stationary and/or dynamical states in above mentioned laser devices. The most complicated of them is resolving temporal-spatial dynamics of full semiconductor equations accounting for microscopic effects and is given by (3+1)-D PDEs (here we denote the three space coordinates plus the time coordinate). [17]. Other less complex three dimensional models are treating some important functionalities phenomenologically and only resolve stationary states. Further simplifications of the model for tapered or broad-area lasers are made by averaging over the vertical y direction. The dynamical (2+1)-D models can be resolved orders of magnitudes faster allowing for parameter studies in acceptable time.

In the present paper we deal with a (2+1)-D dynamical PDE model similar to that one derived in [4, 5, 28]. We note, that some preliminary results were presented in our paper [21]. Here we consider a more general mathematical model and investigate two different numerical algorithms. Both, sequential and parallel versions of these algorithms are considered.

Our model for the optics can be derived starting from the wave equation by assuming a TE polarized electric field (field vector pointing parallel to the x -axis in 1), a stable vertical wave guiding using the effective index method, slowly varying envelopes and a paraxial approximation [4]. In addition to the (1+1)- D longitudinal TW model [5] we take into account the diffraction and diffusion of fields and carriers in the lateral direction (described by Schrödinger and diffusion operators) as well as nonhomogeneous x -dependent device parameters, which capture the geometrical laser design. We are solving the model equations by means of finite-difference (FD) time-domain method.

The main aim of our paper is to make numerical solution of the model as fast as possible, so that two or higher dimensional parameter studies become possible in reasonable time. By discretizing the lateral coordinate we substitute our initial (2+1)-D model by J coupled (1+1)-D TW models [5]. For typical tapered lasers J should be of order $10^2 - 10^3$. Thus, the CPU time needed to resolve (2+1)-D model is by 2 or 3 orders larger than CPU time needed to resolve a simple (1+1)-D TW model.

A possibility to reduce the CPU time is to use a nonuniform mesh in lateral direction. We have implemented this approach in the full FD method and without significant loss of precision were able to reduce the number of grid points (and CPU time) by factor 3. However, such a nonuniform mesh can not be used when applying the split-step method combined with the Fast Fourier Transformation (FFT) approach. In this paper we will consider both techniques, i.e. the FD method combined with the method of characteristics and the split-step method for a separate approximation of the transport, diffraction and nonlinear interaction processes.

Another, very effective way to reduce the computation time is to apply parallel computation techniques. It enables us to solve the given problems faster or/and to solve in real time problems of much larger sizes. In many cases, the latter is most important, since it gives us the possibility to simulate very complex processes with accurate approximations which require solving systems of equations with number of unknowns of order $10^6 - 10^8$ or even more.

The Domain Decomposition (DD) is a general paradigm used to develop parallel algorithms for solution of various applied problems described by systems of PDEs [18, 19]. For numerical algorithms used to solve systems of PDEs usually the general template of such algorithms is fixed. Also, the separation of algorithms itself and data structures used to implement these algorithms can be done. Therefore it is possible to build general purpose libraries and templates which simplify implementation of parallel solvers, e.g. PETSc [2], Diffpack [19] and DUNE [7].

For structured orthogonal grids the data structures used to implement numerical algorithms become even more simple. If the information on the stencil of the grid used to discretize differential equations is known in advance (or determined a posteriori from the algorithm), then it is possible to implement the data exchange among processors automatically. This approach is used in the well known HPF project, which is an extension of Fortran 90 with constructs that support parallel computing. Its most popular implementation is ADAPTOR. This tool is a Fortran compilation system that supports the analysis, translation and optimization of Fortran 90 programs with parallel and/or optimization directives.

The new tool ParSol is targeted for implementation of numerical algorithms in C++ and semi-automatic parallelization of these algorithms on distributed memory parallel computers including clusters of PCs [14]. The library is available on Internet at <http://techmat.vgtu.lt/~alexj/ParSol/>. ParSol presents very efficient and robust implementations of linear algebra objects such as arrays, vectors and matrices [14]. Examples of different problems solved using the ParSol library are given in [13, 15].

In the present work we apply the ParSol library for parallelization of the numerical schemes for broad area or tapered lasers. The numerical experiments were performed on two clusters. The second cluster consists of SMP quad nodes enabling to investigate the efficiency of the proposed parallel algorithm on multicore processors. The algorithm was implemented using MPI library and the same code was used for shared memory data exchange inside SMP node and across distributed memory of different nodes. The development, analysis and implementation of numerical algorithms for solution of the full (2+1)-D dynamical PDE model on parallel computers is the main result of this paper. We demonstrate a speed up of computations by the factor nearly proportional to the number of applied processors.

Our paper is organized as follows. In Section 2 we give a full description of the mathematical model. The finite difference schemes for our model and description of the implementations of the numerical algorithms are given in Section 3. Section 4 describes the parallelization of our algorithms and gives

estimations of the effectiveness of the proposed approach. Results of the numerical simulations of one MOPA example are presented in Section 5. Some final conclusions are done in Section 6.

2 Mathematical Model

The model equations will be considered in the region

$$Q = \{(z, x, t) : (z, x, t) \in (0, L) \times (-X, X) \times (0, T]\},$$

where L is the length of the laser, the interval $(-X, X)$ exceeds the lateral size of the laser and T is the length of time interval where we perform integration. All five parts of the MOPA device compose the closure of the spatial domain: $\bar{Q}_{z,x} = \cup_{j=1}^5 S_j$.

The dynamics of the considered laser device is defined by spatio-temporal evolution of the counter-propagating complex slowly varying amplitudes of optical fields $E^\pm(z, x, t)$, complex dielectric dispersive polarization functions $p^\pm(z, x, t)$ and the real excess carrier density function $N(z, x, t)$. The optical fields are scaled so that

$$P(z, x, t) = |E^+(z, x, t)|^2 + |E^-(z, x, t)|^2$$

represents local photon density at the time moment t . All these functions are governed by the following (2+1)-D traveling wave model:

$$\begin{aligned} \frac{n_g}{c_0} \frac{\partial E^\pm}{\partial t} \pm \frac{\partial E^\pm}{\partial z} = -iD_f \frac{\partial^2 E^\pm}{\partial x^2} - i\beta(N, P)E^\pm - i\kappa^\mp E^\mp \quad (2.1) \\ - \frac{g_p}{2}(E^\pm - p^\pm) + F_{sp}^\pm, \end{aligned}$$

coupled to an ordinary differential equation describing a Lorentzian gain dispersion profile

$$\frac{\partial p^\pm}{\partial t} = i\omega_p p^\pm + \gamma_p(E^\pm - p^\pm), \quad (2.2)$$

and a parabolic diffusion equation for the excess carrier density

$$\begin{aligned} \frac{\partial N}{\partial t} = \frac{\partial}{\partial x} \left(D_N \frac{\partial N}{\partial x} \right) + \frac{J}{ed} - (AN + BN^2 + CN^3) - \\ - \frac{c_0}{n_g} \Re e \left(\sum_{\nu=\pm} E^{\nu*} \left[\frac{G(N)}{1 + \varepsilon P} E^\nu - g_p(E^\nu - p^\nu) \right] \right), \quad (2.3) \end{aligned}$$

where $i = \sqrt{-1}$ and $*$ denotes a complex conjugate.

A propagation factor β is modeled via

$$\beta(N, P) = \delta + \delta_T(J) - \tilde{n}(N) + \frac{i}{2} \left(\frac{G(N)}{1 + \varepsilon P} - \alpha \right).$$

Here, $G(N)$ and $\tilde{n}(N)$ represent the peak gain function and the carrier dependence of the refractive index, respectively:

$$G(N) = g' n_{tr} \log \left(\frac{\max(N, n_*)}{n_{tr}} \right), \quad \tilde{n}(N) = 2\sigma n_{tr} \sqrt{\frac{\max(N, n_*)}{n_{tr}}}, \quad 0 < \frac{n_*}{n_{tr}} \ll 1.$$

A small reference density n_* allows to avoid singularities. g' and σ are differential gain and index change factors of these functions at $N = n_{tr}$. One can also assume any other functional dependence of gain and index change on local carrier density N (see, e.g. [31]).

Function $\delta_T(J)$ represents the refractive index dependency on the injection current induced heating. At the moment¹ we assume the following model of this function [23]:

$$\delta_T(J; x, z)|_{(x,z) \in S_j} = \frac{2\pi n_g}{\lambda_0^2} \sum_{k=1}^5 C_{T,jk} \iint_{S_k} J(x, z) dx dz, \quad j = 1, \dots, 5.$$

Here, the real coefficients $C_{T,jk}$ describe local and nonlocal crosstalk thermal effects due to injection current and all together are defined by a 5×5 real matrix with only few non-vanishing coefficients. The function $J(x, z)$ denotes the injection current density. We assume in our paper that $J(x, z)$ is equally distributed within each laser part S_j , $j = 1, \dots, 5$ and, thus, can be defined by the injection currents I_j into corresponding part S_j :

$$I_j \stackrel{def}{=} \iint_{S_j} J(x, z) dx dz, \quad J(x, z)|_{(x,z) \in S_j} \equiv \frac{I_j}{|S_j|},$$

with $|S_j|$ denoting area of the laser part S_j .

The coefficients κ^\pm , δ , α , ε , n_{tr} , d , A , B and C stand for complex field coupling due to the Bragg grating, static detuning, internal losses of the field, nonlinear gain compression, carrier density at transparency, depth of active zone, and three recombination factors, respectively. Parameters g_p , ω_p and γ_p represent Lorentzian fit of the gain profile in the frequency domain and denote amplitude, central frequency and half width at half maximum of this Lorentzian.

The physical constants c_0 and e correspond to a speed of light in vacuum and an electron charge, respectively. λ_0 is the central wavelength, F_{sp}^\pm in Eq. (2.1) represents a spontaneous emission contribution to optical fields.

Parameters $D_f = \frac{\lambda_0}{4\pi\bar{n}}$ (where \bar{n} is background refractive index) and D_N denote field diffraction and carrier diffusion. In general, they can weakly depend on coordinates x and z . Their dependence on lateral coordinate x makes no difficulties when the given system of PDEs is approximated by the finite difference method and the obtained systems of linear equations are solved by the factorization method. But such a dependence implies great troubles when the split-step Fourier method is used. All other coefficients, with the exception of

¹ A proper modeling of thermal effects would require to resolve corresponding equations with much slower time scales, what sufficiently increase a required computational time.

the group refractive index n_g are allowed to be spatially non-homogeneous and discontinuous depending on the heterostructural laser geometry. For simplicity of notation we are not showing this dependence explicitly. Their more detailed description of all parameters can be found in, e.g., [5, 16]. The standard requirements that the solution and full fluxes of the solution are continuous are formulated on the surfaces of discontinuity of coefficients.

The reflecting boundary conditions of the fields E^\pm at the laser facets $z = 0$ and $z = L$ are defined on $\bar{Q}_{x,t} = [-X, X] \times [0, T]$ as

$$E^+(0, x, t) = r_0(x) E^-(0, x, t), \quad E^-(L, x, t) = r_L(x) E^+(L, x, t), \quad (2.4)$$

where $r_{0,L}$ are complex reflectivity factors, $|r_{0,L}| \leq 1$.

On $\bar{Q}_{z,t} = [0, L] \times (0, T]$ we define the periodic lateral boundary conditions

$$E^\pm(z, -X, t) = E^\pm(z, X, t), \quad N(z, -X, t) = N(z, X, t), \quad (2.5)$$

$$\frac{\partial E^\pm(z, -X, t)}{\partial x} = \frac{\partial E^\pm(z, X, t)}{\partial x}, \quad \frac{\partial N(z, -X, t)}{\partial x} = \frac{\partial N(z, X, t)}{\partial x}. \quad (2.6)$$

Finally, at the initial time moment initial values of the fields, polarizations and carrier densities are defined on $Q_{z,x} = (0, L) \times (-X, X)$ as

$$E^\pm(z, x, 0) = E_{in}^\pm(z, x), \quad p^\pm(z, x, 0) = p_{in}^\pm(z, x), \quad N(z, x, 0) = N_{in}(z, x). \quad (2.7)$$

Well-posedness of the evolution equation (2.1)–(2.3) can be done in a similar way as in [22] by using additional $L^\infty - L^1$ estimates for the Schrödinger semigroup.

3 Discrete Approximations

In this section we present two discrete schemes, which approximate the given system of nonlinear PDEs.

The interval $[-X, X]$ is partitioned non-uniformly by the following grid:

$$\omega_x = \{x_j : j = 0, \dots, J, \quad x_0 = -X, \quad x_J = X, \quad h_{x,j-1/2} = x_j - x_{j-1}\}.$$

Let us define discrete steps $h_z = L/M$, $h_t = T/K$, which are used to define uniform grids with respect to z and t coordinates. The grid points are denoted by $z_i = ih_z$, $t^n = nh_t$. First, we define the main discrete grid in the space (z, x) domain

$$\omega_{zx} = \{(z_i, x_j) : i = 0, \dots, M, \quad x_j \in \omega_x\}.$$

The discretization of problem (2.1)–(2.6) is done on staggered grids (see, Fig. 2):

$$\begin{aligned} \omega_E &= \{(z_i, x_j, t^n) : i = 0, \dots, M, \quad x_j \in \omega_x, \quad n = 0, \dots, K\}, \\ \omega_P &= \{(z_{i-0.5}, x_j, t^n) : i = 1, \dots, M, \quad x_j \in \omega_x, \quad n = 0, \dots, K\}, \\ \omega_N &= \{(z_{i-0.5}, x_j, t^{n-0.5}) : i = 1, \dots, M, \quad x_j \in \omega_x, \quad n = 1, \dots, K\}. \end{aligned}$$

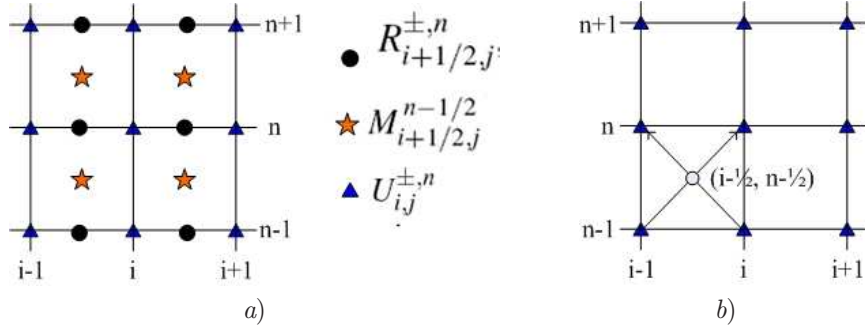


Figure 2. Staggered grids at fixed lateral position x_j : a) the grid points, where discrete functions are defined, b) the characteristics of transport equations (the lateral x -axis is not represented in the figure).

Here subindex i is always an integer number (it should not lead to any misunderstanding with respect to $i = \sqrt{-1}$ in the PDEs of the mathematical model).

Staggered grids are very popular in solving computational fluid dynamic and porous media problems, they are also used to solve nonlinear optics problems [5, 12, 20, 32]. Such a selection of grids allows us to linearize the finite-difference scheme, which approximates a system of nonlinear differential equations.

The discrete functions $U_{i,j}^{\pm,n} = U^{\pm}(z_i, x_j, t^n)$, $R_{i-1/2,j}^{\pm,n} = R^{\pm}(z_{i-1/2}, x_j, t^n)$, and $M_{i-1/2,j}^{n-1/2} = M(z_{i-1/2}, x_j, t^{n-1/2})$ will be used to approximate E^{\pm} , p^{\pm} and N on appropriate grids, respectively (see, Figure 2a).

3.1 Nonlinear finite difference scheme

Approximation of differential equations is done by using the information about the characteristics of transport equations (see Figure 2b) and applying the conservative finite volume averaging for mass conservation.

Discrete transport equations for optical fields. Transport equations (2.1) are approximated along characteristics and time integration is implemented by using the Crank-Nicolson method

$$\begin{aligned} \partial_{ch} U_{i,j}^{\pm,n} = & -iD_f \partial_x \partial_{\bar{x}} \bar{U}_{i-1/2,j}^{\pm,n-1/2} - i\beta \left(M_{i-1/2,j}^{n-1/2}, \bar{P}_{i-1/2,j}^{n-1/2} \right) \bar{U}_{i-1/2,j}^{\pm,n-1/2} \\ & - i\kappa^{\mp} \bar{U}_{i-1/2,j}^{\pm,n-1/2} - \frac{g_p}{2} (\bar{U}_{i-1/2,j}^{\pm,n-1/2} - \bar{R}_{i-1/2,j}^{\pm,n-1/2}) + F_{sp,i-1/2,j}^{\pm,n-1/2}, \end{aligned} \quad (3.1)$$

where we use notation $h_{x,j} = 0.5(h_{x,j-1/2} + h_{x,j+1/2})$,

$$\begin{aligned} \partial_{ch} U_{i,j}^{+,n} &= \frac{U_{i,j}^{+,n} - U_{i-1,j}^{+,n-1}}{h_z}, & \partial_{ch} U_{i,j}^{-,n} &= \frac{U_{i-1,j}^{-,n} - U_{i,j}^{+,n-1}}{h_z}, \\ \bar{U}_{i-1/2,j}^{+,n-1/2} &= \frac{U_{i,j}^{+,n} + U_{i-1,j}^{+,n-1}}{2}, & \bar{U}_{i-1/2,j}^{-,n-1/2} &= \frac{U_{i-1,j}^{-,n} + U_{i,j}^{+,n-1}}{2}, \end{aligned}$$

$$V_{i,j-1/2} := \partial_{\bar{x}} U_{i,j} = \frac{U_{i,j} - U_{i,j-1}}{h_{x,j-1/2}}, \quad \partial_x V_{i,j-1/2} = \frac{V_{i,j+1/2} - V_{i,j-1/2}}{h_{x,j}},$$

$$\bar{R}_{i-1/2,j}^{\pm,n-1/2} = \frac{R_{i-1/2,j}^{\pm,n} + R_{i-1/2,j}^{\pm,n-1}}{2}, \quad \bar{P}_{i-1/2,j}^{n-1/2} = |\bar{U}_{i-1/2,j}^{+,n-1/2}|^2 + |\bar{U}_{i-1/2,j}^{-,n-1/2}|^2.$$

Since the transport equations are approximated along characteristics, we take $h_z = v_g h_t$. Thus the time step h_t depends linearly on the space step h_z , but such a connection enables us to simulate transport along characteristics exactly.

The reflecting boundary conditions (2.4) are approximated by

$$U_{0,j}^{+,n} = r_0(x_j) U_{0,j}^{-,n}, \quad U_{M,j}^{-,n} = r_L(x_j) U_{M,j}^{+,n}, \quad n > 0, \quad 0 \leq j \leq J. \quad (3.2)$$

The periodic lateral boundary conditions are defined as

$$U_{i,0}^{\pm,n} = U_{i,J}^{\pm,n}, \quad U_{i,-1}^{\pm,n} = U_{i,J-1}^{\pm,n}, \quad 0 \leq i \leq M. \quad (3.3)$$

Discrete equations for polarization functions. Equations (2.2) are approximated by the exponentially fitted discrete equations

$$R_{i-1/2,j}^{\pm,n} = e^{-\tilde{\gamma}_p h_t} R_{i-1/2,j}^{\pm,n-1} + \frac{1 - e^{-\tilde{\gamma}_p h_t}}{\tilde{\gamma}_p} \gamma_p \bar{U}_{i-1/2,j}^{\pm,n-1/2}, \quad (3.4)$$

where $\tilde{\gamma}_p = \gamma_p - i\omega_p$.

Discrete equations for the carrier density function. Equation (2.3) is approximated by the Crank-Nicolson type discrete scheme

$$\begin{aligned} \frac{M_{i-1/2,j}^{n+1/2} - M_{i-1/2,j}^{n-1/2}}{h_t} &= \partial_x (D_{N,j-1/2}^H \partial_{\bar{x}} \bar{M}_{i-1/2,j}^n) + \frac{J}{ed} \\ &\quad - \Gamma(\bar{M}_{i-1/2,j}^n) \bar{M}_{i-1/2,j}^n + \varphi_h(\bar{M}_{i-1/2,j}^n, U_{i-1/2,j}^{\pm,n}, R_{i-1/2,j}^{\pm,n}), \end{aligned} \quad (3.5)$$

where we denote

$$\begin{aligned} \bar{M}_{i-1/2,j}^n &= \frac{M_{i-1/2,j}^{n+1/2} + M_{i-1/2,j}^{n-1/2}}{2}, \quad \Gamma(M) = A + BM + CM^2, \\ U_{i-1/2,j}^{\pm,n} &= \frac{1}{2} (U_{i,j}^{\pm,n} + U_{i-1,j}^{\pm,n}), \quad D_{N,i-1/2,j} = D_N(x_j, z_{i-1/2}), \\ D_{N,i-1/2,j-1/2}^H &= 2 \left(\frac{1}{D_{N,i-1/2,j-1}} + \frac{1}{D_{N,i-1/2,j}} \right)^{-1}. \end{aligned}$$

The periodic lateral boundary conditions are defined as

$$M_{i-1/2,0}^{n+1/2} = M_{i-1/2,J}^{n+1/2}, \quad M_{i-1/2,-1}^{n+1/2} = M_{i-1/2,J-1}^{n+1/2}, \quad 1 \leq i \leq M. \quad (3.6)$$

After the standard analysis it follows that the approximation error of the discrete scheme is equal to $\mathcal{O}(h_t^2 + h_z^2 + h_x^2)$, where $h_x = \max_j h_{x,j-1/2}$.

3.2 Linearized numerical algorithm

Discrete scheme (3.1)–(3.6) is nonlinear. For its linearization we use the predictor–corrector algorithm. Substitution of (3.4) into difference equation (3.1) yields the implicit discrete transport equations only for optical fields

$$\begin{aligned} \partial_{ch} U_{i,j}^{\pm,n} &= -iD_f \partial_x \partial_{\bar{x}} \bar{U}_{i-1/2,j}^{\pm,n-1/2} - i\kappa^{\mp} \bar{U}_{i-1/2,j}^{\mp,n-1/2} \\ &\quad - \left(i\beta \left(M_{i-1/2,j}^{n-1/2}, \bar{P}_{i-1/2,j}^{n-1/2} \right) + \frac{g_p}{2} - \frac{g_p \gamma_p (1 - e^{-\tilde{\gamma}_p h t})}{4\tilde{\gamma}_p} \right) \bar{U}_{i-1/2,j}^{\pm,n-1/2} \quad (3.7) \\ &\quad + g_p \left(1 + e^{-\tilde{\gamma}_p h t} \right) R_{i-1/2,j}^{\pm,n-1} / 4 + F_{sp,i-1/2,j}^{\pm,n-1/2}. \end{aligned}$$

For each $i = 1, \dots, M$ Eqs. (3.7) are solved in two steps. In the *predictor* step, we substitute the second argument of the propagation factor β in Eqs. (3.7) by already known value

$$P_{i-1/2,j}^{n-1} = \frac{1}{4} \left(|U_{i-1,j}^{+,n-1} + U_{i,j}^{+,n-1}|^2 + |U_{i,j}^{-,n-1} + U_{i-1,j}^{-,n-1}|^2 \right),$$

and compute the grid function $\tilde{U}_{i,j}^{\pm,n}$, giving an intermediate approximation (*prediction*) for the unknown $U_{i,j}^{\pm,n}$ entering the nonlinear scheme (3.7). In the *corrector* step, we use a corrected photon density approximation

$$\tilde{P}_{i-1/2,j}^{n-1/2} = \frac{1}{4} \left(|U_{i-1,j}^{+,n-1} + \tilde{U}_{i,j}^{+,n}|^2 + |U_{i,j}^{-,n-1} + \tilde{U}_{i-1,j}^{-,n}|^2 \right).$$

Being a second order accurate approximation of the grid function $U_{i,j}^{\pm,n}$, the solution of the resulting linear scheme is used in the consequent computations.

Both prediction and correction steps solve systems of linear equations with a block-tridiagonal matrices. These systems can be written as

$$\begin{cases} \mathcal{A}_0 V_{J-1} + \mathcal{C}_0 V_0 + \mathcal{B}_0 V_1 = \mathcal{D}_0, \\ \mathcal{A}_j V_{j-1} + \mathcal{C}_j V_j + \mathcal{B}_j V_{j+1} = \mathcal{D}_j, \quad 1 \leq j \leq J-2, \\ \mathcal{A}_{J-1} V_{J-2} + \mathcal{C}_{J-1} V_{J-1} + \mathcal{B}_{J-1} V_0 = \mathcal{D}_{J-1}, \end{cases}$$

where $V_j = (\tilde{U}_{i,j}^{+,n}, \tilde{U}_{i-1,j}^{-,n})^T$ for the predictor step and $V_j = (U_{i,j}^{+,n}, U_{i-1,j}^{-,n})^T$ for the corrector step, and $\mathcal{A}_j, \mathcal{B}_j, \mathcal{C}_j$, are 2×2 matrices, and \mathcal{D}_j is a two-component vector containing information about field values at the $(n-1)$ -th time layer. These systems are effectively solved by means of the block version of the factorization algorithm.

The nonlinear scheme (3.5) is also solved in two steps. In the predictor step we substitute the arguments of functions Γ and G by $M_{i-1/2,j}^{n-1/2}$ and compute the grid function $\tilde{M}_{i,j}^{n+1/2}$, giving an intermediate approximation of $M_{i,j}^{n+1/2}$ from nonlinear Eqs. (3.5). In the corrector step these arguments are substituted by $(\tilde{M}_{i-1/2,j}^{n+1/2} + M_{i-1/2,j}^{n-1/2})/2$. The solution of the resulting system of linear equations $M_{i,j}^{n+1/2}$ approximates the exact solution with the second order of accuracy and it is used in the consequent computations. The matrices of both systems of linear equations are tridiagonal, and such systems are solved efficiently by a standard scalar factorization algorithm.

3.3 Split step approximation

In this section we describe the splitting scheme, which approximates the given system of PDEs. The main advantage of this approach that the diffraction and diffusion parts of the problem are resolved separately from the nonlinear interaction and there is no need to solve large systems of linear equations by the factorization (and block-factorization) algorithm. Split step (mostly Fourier based) methods are used in many papers to solve nonlinear optics problems (see, [1, 9, 11, 30, 35]). Here we restrict to a simple first-order accurate approximation, the symmetrical splitting algorithm can be developed by using the standard modifications.

Discrete transport equations for optical fields. In order to approximate the transport equations we use a virtual splitting of the computational domain into to parts: in the first part the diffraction process is taken into account along the characteristics, in the second one the nonlinear interaction takes place. The discrete scheme is written for $x_j \in \omega_x, 0 < i \leq M$:

$$\frac{\hat{U}_{i,j}^{+,n-1/2} - U_{i-1,j}^{+,n-1}}{h_z} + iD_f \partial_x \partial_{\bar{x}} \frac{\hat{U}_{i,j}^{+,n-1/2} + U_{i-1,j}^{+,n-1}}{2} = 0, \tag{3.8}$$

$$\begin{aligned} \frac{U_{i,j}^{+,n} - \hat{U}_{i,j}^{+,n-1/2}}{h_z} &= -i\beta \left(M_{i-1/2,j}^{n-1/2}, \hat{P}_{i,j}^{n-1/2} \right) \frac{U_{i,j}^{+,n} + \hat{U}_{i,j}^{+,n-1/2}}{2} \\ &\quad - i\kappa^- \frac{U_{i,j}^{+,n-1} + \hat{U}_{i,j}^{+,n-1/2}}{2} - \frac{g_p}{2} (U_{i,j}^{+,n} - R_{i,j}^{+,n}) + F_{sp,i-1/2,j}^{+,n-1/2}, \end{aligned} \tag{3.9}$$

$$\begin{aligned} \frac{\hat{U}_{i,j}^{-,n-1/2} - U_{i,j}^{-,n-1}}{h_z} &= -i\beta \left(M_{i-1/2,j}^{n-1/2}, \hat{P}_{i,j}^{n-1/2} \right) \frac{U_{i,j}^{-,n-1} + \hat{U}_{i,j}^{-,n-1/2}}{2} \\ &\quad - i\kappa^+ \frac{U_{i,j}^{+,n} + \hat{U}_{i,j}^{+,n-1/2}}{2} - \frac{g_p}{2} (\hat{U}_{i,j}^{-,n-1/2} - R_{i,j}^{-,n}) + F_{sp,i-1/2,j}^{-,n-1/2}, \end{aligned} \tag{3.10}$$

$$R_{i,j}^{+,n} = e^{-\tilde{\gamma}_p h_t} R_{i,j}^{+,n-1} + \frac{1 - e^{-\tilde{\gamma}_p h_t}}{\tilde{\gamma}_p} \gamma_p \frac{U_{i,j}^{+,n} + \hat{U}_{i,j}^{+,n-1/2}}{2}, \tag{3.11}$$

$$R_{i,j}^{-,n} = e^{-\tilde{\gamma}_p h_t} R_{i,j}^{-,n-1} + \frac{1 - e^{-\tilde{\gamma}_p h_t}}{\tilde{\gamma}_p} \gamma_p \frac{U_{i,j}^{-,n-1} + \hat{U}_{i,j}^{-,n-1/2}}{2}, \tag{3.12}$$

$$\frac{U_{i-1,j}^{-,n} - \hat{U}_{i,j}^{-,n-1/2}}{h_z} + iD_f \partial_x \partial_{\bar{x}} \frac{\hat{U}_{i,j}^{-,n-1/2} + U_{i-1,j}^{-,n}}{2} = 0. \tag{3.13}$$

Here we assume that the discrete grid ω_x is uniform, i.e. $h_{x,j-1/2} = h_x$ and

$$\hat{P}_{i,j}^{n-1/2} = \left| \frac{U_{i,j}^{+,n} + \hat{U}_{i,j}^{+,n-1/2}}{2} \right|^2 + \left| \frac{U_{i,j}^{-,n-1} + \hat{U}_{i,j}^{-,n-1/2}}{2} \right|^2.$$

The solutions $\hat{U}^{+,n-\frac{1}{2}}$, $U_{i-1,j}^{-,n}$ of problems (3.8) and (3.13) are computed efficiently using the FFT algorithm, e.g. the well-known FFTW library [25]. The complexity of solving a system of linear equations by the FFT algorithm is $\mathcal{O}(J \log J)$.

Discrete equations for the carrier density function. If the diffusion coefficient D^H is a constant, then the carrier density equation also can be approximated by the split-type scheme (for all $x_j \in \omega_x$, $0 < i \leq M$):

$$\frac{\hat{M}_{i-1/2,j}^{n+1/2} - M_{i-1/2,j}^{n-1/2}}{h_t} = D^H \partial_x \partial_{\bar{x}} \frac{\hat{M}_{i-1/2,j}^{n+1/2} + M_{i-1/2,j}^{n-1/2}}{2}, \tag{3.14}$$

$$\begin{aligned} \frac{M_{i-1/2,j}^{n+1/2} - \hat{M}_{i-1/2,j}^{n+1/2}}{h_t} &= \frac{J}{ed} - \Gamma(M_{i-1/2,j}^{n+1/2}) \frac{M_{i-1/2,j}^{n+1/2} + \hat{M}_{i-1/2,j}^{n+1/2}}{2} \\ &\quad - \varphi(\bar{M}_{i-1/2}^n, U_{i-1/2}^{\pm,n}, R_{i-1/2}^{\pm,n}). \end{aligned} \tag{3.15}$$

The given nonlinear equations are solved by using the predictor-corrector iterations. By using the Taylor series after simple computations we prove that the approximation error of the proposed split-type scheme is $\mathcal{O}(h_z + h_t + h_x^2)$.

The complexity of the FFT algorithm. The FFT algorithm from the FFTW library is very general and robust. It can be used for any number J of the grid points. But the efficiency of the FFT algorithm depends on J and it is well known that this algorithm is most efficient when $J = 2^m$. In Table 1 we present CPU times obtained in solution of 1D parabolic diffusion problem by using the standard central-differences approximation.

Table 1. CPU times of FFT algorithm for different numbers of the grid points.

J	499	500	511	512	513	560	561	600	1023	1024
CPU	15.3	8.1	13.0	7.9	11.7	9.4	12.1	10.3	26.2	16.9

This information must be taken into account when the discrete grid ω_x is defined. The second possibility, is to add fictitious zero elements in the vectors when the FFT algorithm is applied.

4 Parallel Algorithm

The finite difference scheme is defined on the structured staggered grid and the complexity of computations at each node of the grid is approximately the same. For such problems the parallelization of the algorithm can be done by using domain decomposition (DD) paradigm [18].

4.1 Parallel algorithm

The development of any DD type parallel algorithm requires answers to two main questions. First, we need to select how the domain will be partitioned among processors. At this step the main goal is to preserve the load balance of volumes of subdomains and to minimize the amount of edges connecting grid points of neighbouring subdomains. The last requirement means the minimal costs of data communication among processors during computations. This property is especially important for clusters of PCs, where the ratio between computation and communication rates is not favourable. Let p be the number of processors. It is well known that for 2D structured domains the optimal DD is obtained if 2D topology of processor $p_1 \times p_2$ is used, where $p_j \sim \sqrt{p}$. But for the algorithm (3.7) we can't use such a decomposition straightforwardly since the matrix factorization algorithm for solution of the block three-diagonal system of linear equations is fully sequential in its nature. There are some modifications of the factorization algorithm with much better parallelization properties, but the complexity of such algorithms is at least 2 times larger than the original one (see, e.g. [37]). Thus in this paper we restrict to 1D block domain decomposition algorithms, decomposing the grid only in z direction (see Figure 3).

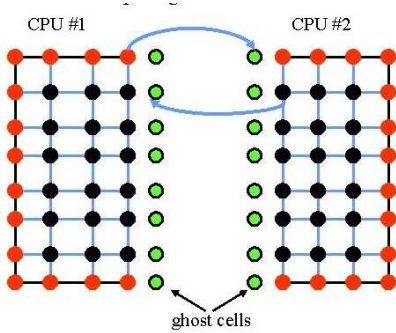


Figure 3. Scheme of the 1D block domain decomposition (distribution with respect to the z coordinate).

The second step in building a parallel algorithm is to define when and what data must be exchanged among processors. This information mainly depends on the stencil of the grid used to approximate differential equations by the discrete scheme. For algorithm (3.7) two different stencils are used to approximate waves moving in opposite directions.

Let us denote by $\omega_z(k)$ the subgrid belonging to the k -th processor

$$\omega_z(k) = \{z_i : i_{kL} \leq i \leq i_{kR}\}.$$

Here the local sub-domains are not overlapping, i.e. $i_{kL} = i_{k-1,R} + 1$.

In order to implement the computational algorithm each processor extends its subgrid by ghost points

$$\tilde{\omega}_z(k) = \{z_i : \tilde{i}_L \leq i \leq \tilde{i}_R\}, \quad \tilde{i}_L = \max(i_L - 1, 0), \quad \tilde{i}_R = \min(i_R + 1, M).$$

Then after each predictor and corrector substeps, the k -th processor

- sends to $(k+1)$ -th processor vector $U_{i_R}^+$, and receives from him vector $U_{\tilde{i}_R}^-$,

- sends to $(k-1)$ -th processor vector $U_{i_L, \cdot}^-$ and receives from him vector $U_{i_L, \cdot}^+$.

Obviously, if $k = 0$ or $k = (p-1)$, then a part of communications is not done. We note that vectors $R_{i-\frac{1}{2}, \cdot}^+$, $M_{i-\frac{1}{2}, \cdot}^-$ are computed locally by each processor and no communications of values at ghost points are required.

4.2 Scalability analysis

In this section we will estimate the complexity of the parallel algorithm. Neglecting the work done to update the boundary conditions on ω_{zx} we get that the complexity of the serial algorithm for one time step is given by $W = \gamma M(J+1)$, where γ estimates the CPU time required to implement one basic operation of the algorithm.

The ParSol tool distributes among processors the grid ω_{zx} using 1D type distribution with respect the z coordinate. The total size of this grid is $(M+1)(J+1)$ points. Then the computational complexity of parallel algorithm depends on the size of largest local grid part, given to one processor. It is equal to

$$T_{p,comp} = \gamma([\!(M+1)/p\!] + 1)(J+1),$$

where $\lceil x \rceil$ denotes a smallest integer number larger or equal to x . This formula includes costs of extra computations involving ghost points.

Data communication time is given by $T_{p,comm} = 2(\alpha + \beta(J+1))$, here α is the message startup time and β is the time required to send one element of data. We assume that communication between neighbouring processors can be implemented in parallel. Thus the total complexity of the parallel algorithm is equal to

$$T_p = \gamma([\!(M+1)/p\!] + 1)(J+1) + 2(\alpha + \beta(J+1)). \quad (4.1)$$

The scalability analysis of any parallel algorithm enables us to find the rate at which the size of problem W needs to grow with respect to the number of processors p in order to maintain a fixed efficiency E of the algorithm. Let $H(p, W) = pT_p - W$ be the total overhead of a parallel algorithm. Then the *isoefficiency* function $W = g(p, E)$ is defined by the implicit equation [18]:

$$W = \frac{E}{1-E} H(p, W). \quad (4.2)$$

The total overhead of the proposed parallel algorithm is given by

$$H(p, W) = \gamma(p+1)(J+1) + 2\alpha p + 2\beta p(J+1).$$

After simple computations we get from (4.2) the following isoefficiency function, expressed with respect to the number of grid points in z coordinate:

$$M = \frac{E}{1-E} \left[\left(1 + 2\frac{\beta}{\gamma} + 2\frac{\alpha}{\gamma(J+1)} \right) p + 1 \right].$$

Thus in order to maintain a fixed efficiency E of the parallel algorithm it is sufficient to preserve the same number of grid $\omega_z(k)$ points per processor. The increase of J reduces the influence of the message startup time.

4.3 Computational experiments

In this paper we restrict to computational experiments which are targeted for the efficiency and scalability analysis of the given parallel algorithm. Results of extensive computational experiments for simulation of the dynamics of multisection semiconductor lasers and analysis of their stability domain will be presented in a separate paper.

We have solved the problem (2.1)–(2.6) by using the discrete approximation (3.1)–(3.6). The dynamics of laser waves was simulated till 0.2 ns. The discretization was done on three discrete grids of $(M + 1) \times (J + 1)$ elements, with $(M = 500, J = 300)$, $(M = 500, J = 600)$ and $(M = 1000, J = 600)$ respectively. Note, that an increase of M implies a proportional increase of the time steps K within the interval of computations.

The parallel algorithm was implemented by using the mathematical objects library ParSol [14]. This tool not only implements some important linear algebra objects in C++, but also allows to parallelize semi-automatically data parallel algorithms, similarly to HPF.

First, the parallel code was tested on the cluster of PCs at Vilnius Gediminas technical university. It consists of Pentium 4 processors (3.2 GHz, level 1 cache 16 kB, level 2 cache 1 MB) interconnected via Gigabit Smart Switch (<http://vilkas.vgtu.lt>). Obtained performance results are presented in Table 2. Here for each number of processors p the coefficients of the algorithmic speed up $S_p = T_1/T_p$ and efficiency $E_p = S_p/p$ are presented. T_p denotes the CPU time required to solve the problem using p processors and the following results were obtained for the sequential algorithm (in seconds):

$$T_1(500 \times 300) = 407.3, \quad T_1(500 \times 600) = 814.2, \quad T_1(1000 \times 600) = 3308.4.$$

Table 2. Results of computational experiments on Vilkas cluster.

	$p = 1$	$p = 2$	$p = 4$	$p = 8$	$p = 16$
$S_p(500 \times 300)$	1.0	1.93	3.81	7.42	14.2
$E_p(500 \times 300)$	1.0	0.97	0.95	0.93	0.90
$S_p(500 \times 600)$	1.0	1.93	3.80	7.43	14.4
$E_p(500 \times 600)$	1.0	0.97	0.95	0.93	0.90
$S_p(1000 \times 600)$	1.0	1.94	3.82	7.62	14.9
$E_p(1000 \times 600)$	1.0	0.97	0.96	0.95	0.93

Table 3. Results of computational experiments on Hercules cluster.

	1×1	2×1	1×2	4×1	1×4	8×1	2×4	4×4	8×4
S_p	1.0	1.88	1.95	3.94	3.40	7.97	7.22	14.96	29.2
E_p	1.0	0.94	0.97	0.99	0.85	0.99	0.90	0.93	0.91

Table 4. Parameters used in simulations.

Symbol	Description	Unit	Value
λ_0	central wavelength	m	$973 \cdot 10^{-9}$
n_g	group refractive index		3.66
d	depth of the active zone	m	$16 \cdot 10^{-9}$
D_f	field diffraction coef.	m	$24 \cdot 10^{-9}$
D_N	carrier diffusion coefficient	$m^2 s^{-1}$	$20 \cdot 10^{-4}$
r_0	(complex) rear facet field reflectivity		-0.04
r_L	(complex) front facet field reflectivity		0.04
l_1	length of S_1 (MO)	m	$2 \cdot 10^{-3}$
l_2	length of S_2 (PA)	m	$2 \cdot 10^{-3}$
w_1	width of S_1 & inner edge of S_2	m	$2.5 \cdot 10^{-6}$
w_2	width of S_2 at front facet	m	$2.1 \cdot 10^{-4}$
κ	field coupling in S_1	m^{-1}	250
	in $S_{2,3,4,5}$	m^{-1}	0
g'	differential gain in $S_{1,2,3,4}$	m^2	$1.8 \cdot 10^{-21}$
	in S_5	m^2	0
σ	differential index in $S_{1,2,3,4}$	m^2	$1.8 \cdot 10^{-21}$
	in S_5	m^2	0
α	internal absorption in $S_{1,2,3,4}$	m^{-1}	150
	in S_5	m^{-1}	3000
δ	index step detuning in S_3 (trench)	m^{-1}	-32000
	in $S_{1,2,4,5}$	m^{-1}	0
n_{tr}	transparency carrier density	m^{-3}	$1.3 \cdot 10^{24}$
ϵ	nonlinear gain compression	m^3	0
A	inverse carrier life time	s^{-1}	$3 \cdot 10^8$
B	bimolecular recombination coef.	$m^3 s^{-1}$	$1.8 \cdot 10^{-16}$
C	Auger recombination coef.	$m^6 s^{-1}$	$3 \cdot 10^{-42}$
g_p	Lorentzian gain amplitude	m^{-1}	13000
$2\gamma_p$	Lorentzian width at half max.	s^{-1}	$50\pi \cdot 10^{12}$
ω_p	gain peak detuning	s^{-1}	$\pi \cdot 10^{12}$
I	injection current into S_1 (MO)	A	0.4
	into S_2 (PA)	A	[3, 3.2]
	into $S_{3,4,5}$	A	0
$C_{T,jl}$	thermal coefficient, $j = l = 1$	$A^{-1}m$	$3.2 \cdot 10^{-9}$
	$j = l = 2$	$A^{-1}m$	$0.8 \cdot 10^{-9}$
	$j = 1, l = 2$	$A^{-1}m$	$0.1 \cdot 10^{-9}$
	$j = 2, l = 1$	$A^{-1}m$	$0.1 \cdot 10^{-9}$
	other	$A^{-1}m$	0

We see that experimental results scale according the theoretical complexity analysis prediction given by (4.1). For example, the efficiency of the parallel algorithm satisfies the estimate $E_{2p}(1000 \times 600) \approx E_p(500 \times 600)$.

Next we present results obtained on the Hercules cluster in ITWM, Germany. It consists of dual Intel Xeon 5148LV nodes (i.e., 4 CPU cores per node), each node has 8 GB RAM, 80 GB HDD, the nodes are interconnected by 2x Gigabit Ethernet, Infiniband. In Table 3 the values of the speed-up and efficiency coefficients are presented for the discrete problem simulated on the discrete grid of size 640×400 and different configurations of nodes. In all cases the nodes were used in the dedicated to one user mode. We denote by $n \times m$ the configuration, where n nodes are used with m processes on each node.

It follows from the presented results that the proposed parallel algorithm efficiently runs using both computational modes of the given cluster. In the case of $p \times 1$ configuration the classical cluster of the distributed memory is

obtained, and in the case of $n \times m$ configuration the mixture model of the global memory inside one node and distributed memory across the different nodes is used. It seems that the usage of L1 and L2 cache memory also improved for larger numbers of processes, when smaller local problems are allocated to each node.

5 Results of Numerical Simulations

In this section we present results of numerical simulation of an example of the MOPA laser represented in Fig. 1, modeled by Eqs. (2.1)–(2.7) and defined by parameters given in Table 4, which are similar to those used in [23].

The resolution of the waveguiding within the MO (S_1) requires a sufficiently fine lateral space discretization. Similarly, a proper propagation of the fast oscillating modes along the characteristics as well as the resolution of a sufficiently large optical frequency range requires a fine time- and longitudinal space discretization. In our case we have used a uniform spatial grid with the steps $\Delta x = 0.625\mu\text{m}$, $\Delta z = 5\mu\text{m}$, resulting in a time step of $\sim 0.061\text{ps}$. This spatial grid has 320000 nodes, yielding 2.88 million real unknown variables.

Typical simulated spatial distributions of forward and backward propagating optical field intensities and carrier density of the stationary (rotational wave) state at some fixed time instant t are represented in Fig. 4.

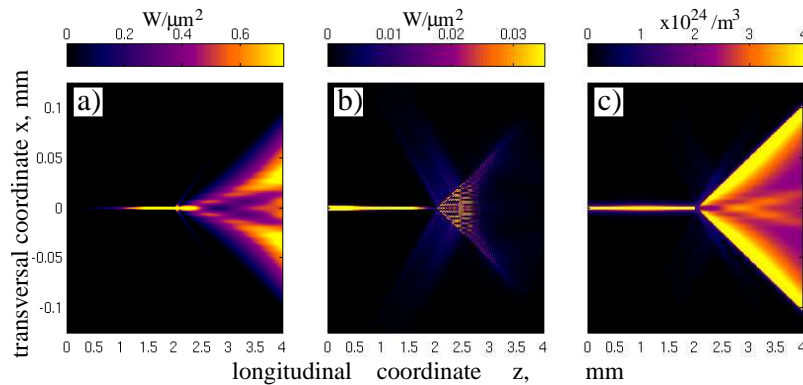


Figure 4. Spatial distributions of forward and backward field intensities (a,b) and carriers (c) at the stable CW state. The injection currents $I_1 = 0.4\text{ A}$ and $I_2 = 3\text{ A}$, respectively.

The first two panels show local field intensities (per m^2 transversal cross-section of the active zone) $|\tilde{E}^\pm(z, x, t)|^2$ which are equal to the local field densities $|E^\pm(z, x, t)|^2$ multiplied by $\frac{hc_0^2}{n_g \lambda_0}$ (h : Planck constant). Panel (a) shows propagation and amplification of the optical field E^+ . The largest intensity of this field is achieved at the left edge of the PA section ($z = L$), where it is emitted from the laser. Obviously, the residual reflection $r_L \neq 0$ implies the presence and amplification of the field E^- within the PA (see panel b, and causes feedback to the MO, with dramatic consequences, as we will show.

Strong intensity variations cause spatial hole burning of carriers within the PA section of the device (see panel *c*).

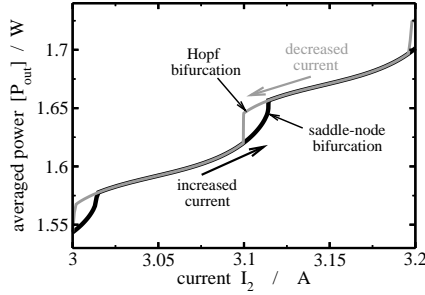


Figure 5. Averaged output field intensity $[P_{out}]$ of the stable orbits obtained with increasing (black) and decreasing (grey) injection current I_2 .

In Fig. 5 we present the one-parameter continuation of stable orbits with increasing and decreasing injection current I_2 . Namely, in this figure we show changes of the temporal average $[P_{out}]$ of the field intensity $P_{out}(t)$ outgoing from the PA facet. Here,

$$P_{out}(t) = d \int_{-X}^X (1 - |r_L|^2) |\tilde{E}^+(L, x, t)|^2 dx, \quad |P_{out}| = \frac{1}{T} \int_{t_{in}}^{t_{in}+T} P_{out}(t) dt.$$

Our simulations were performed as follows. First, we fix currents $I_1 = 0.4$ A, $I_2 = 3$ A and integrate numerically the model equations (2.1)–(2.7) with arbitrary selected initial distributions $E_{in}^{\pm}(z, x)$, $p_{in}^{\pm}(z, x)$ and $N_{in}(z, x)$ over several nanoseconds. During this transient the computed trajectory is approaching some stable orbit (a stationary state in our case). Neglecting a small difference between the computed trajectory and the stable orbit at the end of this transient, we estimate the averaged output field intensity $\langle P_{out} \rangle$ of this orbit from the last 1 ns of our computations. In the following steps we adjust the initial distributions E_{in}^{\pm} , p_{in}^{\pm} and N_{in} to the corresponding distributions obtained at the last time moment of previous integration and increase injection I_2 by 0.001 A until $I_2 \leq 3.2$ A. After each change of I_2 we integrate numerically the model equations over 4 ns and the last 1 ns use for the estimation of $\langle P_{out} \rangle$ of the actual attracting orbit. Similarly we perform our simulations when decreasing injection current I_2 from 3.2 A down to 3 A with a step of 0.001 A.

The small change of parameter implies also changes of the previously estimated orbit. When the changes of this orbit are small, it can be easily approached by the computed trajectory during considered 4 ns transient. However, sometimes small parameter changes imply transitions to qualitatively different orbits. One of such bifurcations for increased current I_2 is observed at $I_2 \approx 3.114$ A: see black curve in Fig. 5. The inspection of the changing optical spectra and the bifurcation analysis of the similar narrow waveguide multisection edge-emitting semiconductor lasers [6, 31, 34] allows us to identify it as a saddle-node bifurcation. This suggestion is supported also by the type of transient $P_{out}(t)$ just before the bifurcation (see Fig. 6a), since there is

no for semiconductor lasers typical relaxation oscillations during the transition towards the stationary state.

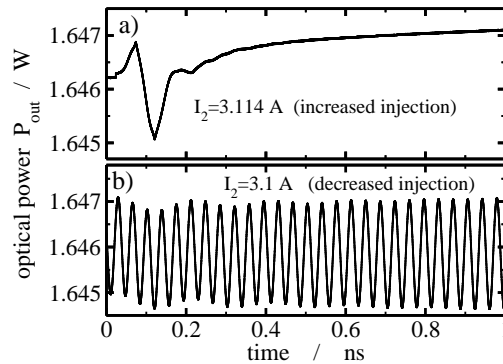


Figure 6. Time traces of the output field intensity P_{out} just before saddle-node (a) and just after Hopf (b) bifurcations, occurring with the increasing and decreasing injection current I_2 .

When decreasing I_2 (grey curve in Fig. 5) we could observe different bifurcations. First, slightly before $I_2 = 3.1A$ we have the supercritical Hopf bifurcation of the stationary state, which can be easily recognized from the transients of $P_{out}(t)$. Part of such transient at $I_2 = 3.1A$ is shown in Fig. 6b. Here the trajectory is repelled from now unstable stationary state and is approaching some newly born stable limit cycle. The norm $\langle P_{out} \rangle$ of this limit cycle, however, is similar to that one of the stationary state, and, therefore, Fig. 5 does not provide a direct indication of this bifurcation. On the other hand, this figure clearly shows another bifurcation at slightly smaller I_2 . Here the stable limit cycle loses its stability and the transition of the computed trajectory towards the stable stationary state occurs.

To perform 1-parameter continuation shown in Fig. 5 we have integrated the model equations over $\approx 1600ns$. The parallelization of our algorithm has allowed to perform these simulations on a blade cluster of 64 quad core Intel Xeon5430 processors interconnected via Infiniband (HP CP3000BL 32xHP BL460c) during a single day. Comparable computations on a single PC system would take nearly 100 times longer.

6 Conclusions

The new parallel algorithm for simulation of the dynamics of high-power semiconductor lasers is presented. The codes implement second order accurate in space and time finite-difference scheme and the first order accurate split step Fourier method based discrete scheme. It uses a domain decomposition parallelization paradigm for the effective partitioning of the computational domain. The parallel algorithm is implemented by using ParSol tool, which uses MPI for data communication. The computational experiments carried out have shown the scalability of the code in different clusters including SMP nodes with 4 cores.

Further studies must be carried out to test 2D data decomposition model in order to reduce the amount of data communicated during computations.

Acknowledgement

R. Čiegis was supported by the Lithuanian State Science and Studies Foundation within the project on B-03/2008 "Global optimization of complex systems using high performance computing and GRID technologies". The work of M. Radziunas was supported by DFG Research Center MATHEON "Mathematics for key technologies: Modelling, simulation and optimization of the real world processes".

References

- [1] G.P. Agrawal. *Nonlinear Fiber Optics*. Academic, London, UK, 1995.
- [2] S. Balay, K. Buschelman, V. Eijkhout, W.D. Gropp, Kaushik W.D., M.G. Knepley, L. Curfman McInnes, B.F. Smith and H. Zhang. *PETSc Users Manual. ANL-95/11 – Revision 2.3.0*. Argonne National Laboratory, 2005.
- [3] S. Balsamo, G. Ghisloti, F. Trezzi, P. Bravetti, G. Coli and S. Morasca. High-power 980-nm pump lasers with flared waveguide design. *J. Lightw. Technol.*, **20**(8):1512–1516, 2002.
- [4] S. Balsamo, F. Sartori and I. Montrosset. Dynamic beam propagation method for flared semiconductor power amplifiers. *IEEE Journal of Selected Topics in Quantum Electronics*, **2**:378–384, 1996.
- [5] U. Bandelow, M. Radziunas, J. Sieber and M. Wolfrum. Impact of gain dispersion on the spatio-temporal dynamics of multisection lasers. *IEEE J. Quantum Electron.*, **37**(2):183–188, 2001.
- [6] S. Bauer, O. Brox, J. Kreissl, B. Sartorius, M. Radziunas, J. Sieber, H.-J. Wünsche and F. Henneberger. Nonlinear dynamics of semiconductor lasers with active optical feedback. *Phys. Rev. E*, **69**(1):206–215, 2004.
- [7] M. Blatt and P. Bastian. The iterative solver template library. In B.Kagstrom, E. Elmroth, J. Dongarra and J. Wasniewski(Eds.), *Lecture Notes in Scientific Computing. Applied Parallel Computing, State of the Art in Scientific Computing*, volume 4699, pp. 666–675, Berlin, Heidelberg, New York, 2007. Springer.
- [8] L. Borruel, S. Sujecki, P. Moreno, J. Wykes, P. Sewell, T.M. Benson, E.C. Larkins and I. Esquivias. Modeling of patterned contacts in tapered lasers. *IEEE J. Quantum Electron.*, **40**:1384–1388, 2004.
- [9] J.M. Burzler, S. Hughes and B.S. Wherrett. Split-step Fourier methods applied to model nonlinear refractive effects in optically thick media. *Applied Physics B: Lasers and Optics*, **62**(4):389–397, 1996.
- [10] P. Chazan, J.M. Mayor, S. Morgott, M. Mikulla, R. Kiefer, S. Müller, M. Walther, J. Braunstein and G. Weimann. High-power near diffraction-limited tapered amplifiers at 1064 nm for optical intersatellite communications. *IEEE Phot. Techn. Lett.*, **10**(11):1542–1544, 1998.
- [11] R. Čiegis. Numerical simulation of nonlinear phase conjugation process. *Informatika*, **1**(1):3–19, 1990.

- [12] R. Čiegis, A. Dementev and G. Jankevičiūtė. Numerical analysis of hyperbolic two temperature model. *Lithuanian Mathematical Journal*, **48**(1):46–60, 2008.
- [13] R. Čiegis, A. Jakušev, A. Krylovas and O. Suboč. Parallel algorithms for solution of nonlinear diffusion problems in image smoothing. *Math. Mod. and Anal.*, **10**(2):155–172, 2005.
- [14] R. Čiegis, A. Jakušev and V. Starikovičius. Parallel tool for solution of multi-phase flow problems. In R. Wyrzykowski, J. Dongarra, N. Meyer and J. Wasniewski(Eds.), *Lecture notes in computer science. Sixth International conference on Parallel Processing and Applied Mathematics. Poznan, Poland, September 10-14, 2005*, volume 3911, pp. 312–319, Berlin, Heidelberg, New York, 2006. Springer.
- [15] Raim. Čiegis, Rem. Čiegis, A. Jakušev and G. Šaltenienė. Parallel variational iterative algorithms for solution of linear systems. *Math. Mod. and Anal.*, **12**(1):1–16, 2007.
- [16] A. Egan, C. Z. Ning, J. V. Moloney, R. A. Indik, M. W. Wright, D. J. Bossert and J. G. McInerney. Dynamic instabilities in master oscillator power amplifier semiconductor lasers. *IEEE J. Quantum Electron.*, **34**(1):166–170, 1998.
- [17] E. Gehrig, O. Hess and R. Walenstein. Modeling of the performance of high power diode amplifier systems with an optothermal microscopic spatio-temporal theory. *IEEE J. Quantum Electron.*, **35**:320–331, 2004.
- [18] V. Kumar, A. Grama, A. Gupta and G. Karypis. *Introduction to Parallel Computing: Design and Analysis of Algorithms*. Benjamin/Cummings, Redwood City, 1994.
- [19] H.P. Langtangen. *Computational Partial Differential Equations. Numerical Methods and Diffpack Programming*. Springer, Berlin, 2002.
- [20] I. Laukaitytė and R. Čiegis. Finite-difference scheme for one problem of nonlinear optics. *Math. Mod. and Anal.*, **13**(2):211–222, 2008.
- [21] I. Laukaitytė, R. Čiegis, M. Lichtner and M. Radziunas. Parallel numerical algorithm for the traveling wave model. In R. Čiegis, D. Henty, B. Kagström and J. Žilinskas(Eds.), *Parallel Linear Algebra and Optimization: Advances and Applications. Springer Optimization and Its Applications. ISBN: 978-0-387-09706-0*, volume 27, pp. 241–256, New-York, 2009. Springer.
- [22] M. Lichtner, M. Radziunas and L. Recke. Well posedness, smooth dependence and center manifold reduction for a semilinear hyperbolic system from laser dynamics. *Math. Meth. Appl. Sci.*, **30**:931–960, 2007.
- [23] M. Lichtner and M. Spreemann. *Parallel simulation of high power semiconductor lasers*. WIAS Preprint, no. 1326, Berlin, Germany: WIAS, 2008.
- [24] J.J. Lim, T.M. Benson and E.C. Larkins. Design of wide-emitter single-mode laser diodes. *IEEE J. Quantum Electron.*, **41**:506–516, 2005.
- [25] S.G. Johnson M. Frigo. The design and implementation of fftw3. *Proceedings of the IEEE*, **93**(2):216–231, 2005.
- [26] M. Maiwald, S. Schwertfeger, R. Güther, B. Sumpf, K.Paschke, C. Dzionk, G. Erbert and G. Tränkle. 600 mw optical output power at 488 nm by use of a high-power hybrid laser diode system and a periodically poled MgO:LiNbO₃. *Optics Letters*, **31**(6):802–804, 2006.
- [27] J.R. Marciante and G.P. Agrawal. Nonlinear mechanisms of filamentation in broad-area semiconductor lasers. *IEEE J. Quantum Electron.*, **32**:590–596, 1996.

- [28] C.Z. Ning, R.A. Indik and J.V. Moloney. Effective Bloch equations for semiconductor lasers and amplifiers. *IEEE J. Quantum Electron.*, **33**:1543–1550, 1997.
- [29] M. Pessa, J. Näppi, P. Savolainen, M. Toivonen, R. Murison, A. Ovchinnikov and H. Asonen. State-of-the-art aluminum-free 980-nm laser diodes. *J. Lighthw. Technol.*, **14**(10):2356–2361, 1996.
- [30] M. Premaratne. Split-step spline method for modeling optical fiber communications systems. *IEEE Photonics Technology Letters*, **16**(5):1304–1306, 2004.
- [31] M. Radziunas. Numerical bifurcation analysis of the traveling wave model of multisection semiconductor lasers. *Physica D*, **213**:98–112, 2006.
- [32] M. Radziunas and H.J. Wünsche. Multisection lasers: longitudinal modes and their dynamics. In J. Piprek(Ed.), *Optoelectronic Devices-Advanced Simulation and Analysis*, pp. 121–150, New York, 2004. Springer Verlag.
- [33] W. Schultz and R. Poprawe. Manufacturing with novel high-power diode lasers. *IEEE J. Select. Topics Quantum Electron.*, **6**(4):696–705, 2000.
- [34] J. Sieber. Numerical bifurcation analysis for multi-section semiconductor lasers. *SIAM J. Appl. Dyn. Syst.*, **1**:248–270, 2002.
- [35] O. Sinkin, R. Holzlöhner, J. Zweck and C. Menyuk. Optimization of the split-step Fourier method in modelling optical fiber communications systems. *IEEE J. of Lightwave Technol.*, **21**:61–88, 2003.
- [36] P.M. Skovgaard, J.G. McInerney, J.V. Moloney, R.A. Indik and C.Z. Ning. Enhanced stability of MFA-MOPA semiconductor lasers using a nonlinear, trumpet-shaped flare. *IEEE Phot. Techn. Lett.*, **9**(9):1220–1222, 1997.
- [37] H.H. Wang. A parallel method for tridiagonal equations. *ACM Transactions on Mathematical Software*, **7**(2):170–183, 1981.
- [38] H. Wenzel, B. Sumpf and G. Erbert. High-brightness diode lasers. *C. R. Physique*, **4**:649–661, 2003.